Comparison of electromagnetic and nuclear dissociation of Ne 17

Comparison of electromagnetic and nuclear dissociation of ^{17}Ne

F. Wamers,[1,2] J. Marganiec,[1,2,3] F. Aksouh,[1,4] Yu. Aksyutina,[1] H. Alvarez-Pol,[5] T. Aumann,[2,1] S. Beceiro-Novo,[5] C. A. Bertulani,[6] K. Boretzky,[1] M. J. G. Borge,[7] M. Chartier,[8] A. Chatillon,[1] L. V. Chulkov,[9,1] D. Cortina-Gil,[10] H. Emling,[1] O. Ershova,[1,11] L. M. Fraile,[12] H. O. U. Fynbo,[13] D. Galaviz,[7] H. Geissel,[1] M. Heil,[1] D. H. H. Hoffmann,[2] J. Hoffman,[1] H. T. Johansson,[14] B. Jonson,[14] C. Karagiannis,[1] O. A. Kiselev,[1] J. V. Kratz,[15] R. Kulessa,[16] N. Kurz,[1] C. Langer,[1,11] M. Lantz,[17] T. Le Bleis,[1] C. Lehr,[2] R. Lemmon,[18] Yu. A. Litvinov,[1] K. Mahata,[1] C. Müntz,[1] T. Nilsson,[14] C. Nociforo,[1] W. Ott,[1] V. Panin,[2,1] S. Paschalis,[8,19] A. Perea,[7] R. Plag,[1,11] R. Reifarth,[1,11] A. Richter,[2] K. Riisager,[13] C. Rodriguez-Tajes,[10] D. Rossi,[2,1] D. Savran,[3,20] G. Schrieder,[2] H. Simon,[1] J. Stroth,[11] K. Sümmerer,[1] O. Tengblad,[7] S. Typel,[2,1] H. Weick,[1] M. Wiescher,[21] and C. Wimmer[1,11]

[1]*GSI Helmholtzzentrum für Schwerionenforschung GmbH, D-64291 Darmstadt, Germany*
[2]*Institut für Kernphysik, Technische Universität, D-64289 Darmstadt, Germany*
[3]*ExtreMe Matter Institute, EMMI, D-64291 Darmstadt, Germany*
[4]*Physics & Astronomy Department, College of Sciences, King Saud University, Riyadh SA-2455, Saudi Arabia*
[5]*Departamento de Física de Partículas, Universidade de Santiago de Compostela, ES-15782 Santiago de Compostela, Spain*
[6]*Department of Physics and Astronomy, Texas A&M University-Commerce, Texas 75429, USA*
[7]*Instituto de Estructura de la Materia, CSIC, ES-28006 Madrid, Spain*
[8]*Department of Physics, University of Liverpool, Liverpool L69 3BX, United Kingdom*
[9]*NRC Kurchatov Institute, RU-123182 Moscow, Russia*
[10]*Universidade de Santiago de Compostela, 15782 Santiago de Compostela, Spain*
[11]*Institut für Angewandte Physik, Goethe Universität, D-60438 Frankfurt am Main, Germany*
[12]*Department of Atomic, Molecular and Nuclear Physics, Universidad Complutense de Madrid, ES-28040 Madrid, Spain*
[13]*Department of Physics and Astronomy, University of Aarhus, DK-8000 Aarhus, Denmark*
[14]*Fysiska institutionen, Chalmers Tekniska Högskola, SE-41296 Göteborg, Sweden*
[15]*Institut für Kernchemie, Johannes Gutenberg-Universität Mainz, D-55122 Mainz, Germany*
[16]*Instytut Fisiki, Uniwersytet Jagelloński, PL-30-059 Krakóv, Poland*
[17]*Instututionen för fysik och astronomi, Uppsala Universitet, SE-75120 Uppsala, Sweden*
[18]*Nuclear Physics Group, STFC Daresbury Lab, Warrington WA4 4AD, Cheshire, United Kingdom*
[19]*Department of Physics, University of York, York YO10 5DD, United Kingdom*
[20]*Frankfurt Institute for Advanced Studies FIAS, D-60438 Frankfurt am Main, Germany*
[21]*JINA, University of Notre Dame, Indiana 46556 Notre Dame, USA*

(Received 18 December 2017; published 20 March 2018)

The Borromean drip-line nucleus ^{17}Ne has been suggested to possess a two-proton halo structure in its ground state. In the astrophysical rp-process, where the two-proton capture reaction $^{15}\mathrm{O}(2p,\gamma)^{17}\mathrm{Ne}$ plays an important role, the calculated reaction rate differs by several orders of magnitude between different theoretical approaches. To add to the understanding of the ^{17}Ne structure we have studied nuclear and electromagnetic dissociation. A 500 MeV/u ^{17}Ne beam was directed toward lead, carbon, and polyethylene targets. Oxygen isotopes in the final state were measured in coincidence with one or two protons. Different reaction branches in the dissociation of ^{17}Ne were disentangled. The relative populations of s and d states in ^{16}F were determined for light and heavy targets. The differential cross section for electromagnetic dissociation (EMD) shows a continuous internal energy spectrum in the three-body system $^{15}\mathrm{O}+2p$. The ^{17}Ne EMD data were compared to current theoretical models. None of them, however, yields satisfactory agreement with the experimental data presented here. These new data may facilitate future development of adequate models for description of the fragmentation process.

DOI: 10.1103/PhysRevC.97.034612

I. INTRODUCTION

The investigation of nuclear structure and reaction mechanisms for light drip-line nuclei, using intense radioactive beams, is one of the current frontiers of experimental and theoretical nuclear physics [1]. The halos discovered in light drip-line nuclei are fascinating structural phenomena characterized by low separation energies of the valence nucleons in low-angular momentum states. These features result in an extended valence-nucleon wave function far beyond the range of the nucleon-core potential. Traditional shell-model and mean-field models break down, as can be expected in such a dilute structure, while cluster models can reproduce the most general features. Numerous nuclei possessing a

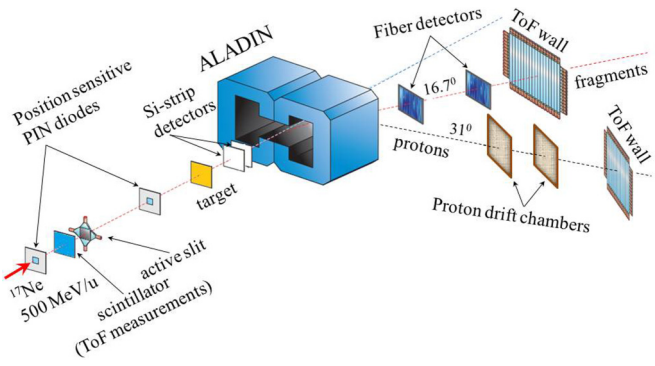

FIG. 1. Schematic outline of the experimental setup.

neutron-halo structure are observed among light neutron-rich drip-line nuclei ($Z \leqslant 10$) [2]. There are, however, only a few proton-halo nuclei or candidates for such. Evidence of one-proton halos has been found for ^{8}B(g.s.) [3] [$S_p = 136(4)$ keV, p shell], for an excited state ^{17}F($1/2^+$) [4] [$S_p = 104.9(3)$ keV, s shell], and for ^{12}N(g.s.) [5] [$S_p = 601.2(1.4)$ keV, p shell]. The ^{17}Ne nucleus is the only realistic candidate for having a two-proton halo [5,6] [$S_{2p} = 933.1(0.6)$ keV, sd shell]. The proton separation energies given here were taken from Ref. [7]. The properties of ^{17}Ne have been intensively studied both theoretically and experimentally. However, these investigations give contradicting results both in the analyses of experimental data and in the theoretical predictions (see Refs. [8,9] and references therein).

Experimental data for drip-line nuclei are also important ingredients in astrophysical calculations, such as nucleosynthesis, stellar evolution, and supernova dynamics. Here an understanding of the ^{17}Ne electromagnetic dissociation is of relevance for the rapid proton-capture rp-process, where ^{15}O ($T_{1/2} = 122$ s) is a waiting-point nucleus to produce heavier elements and the two-proton capture reaction ^{15}O$(2p,\gamma)^{17}$Ne is expected to compete with other reaction branches. However, theoretical calculations of the ^{15}O$(2p,\gamma)^{17}$Ne reaction rate differ by several orders of magnitude among each other [10–12].

The purpose of the present paper is to present new experimental data on nuclear and electromagnetic dissociation of ^{17}Ne to further elucidate its structure.

II. EXPERIMENT

The present experiment was performed at the GSI Helmholzzentrum für Schwerionenforschung GmbH in Darmstadt, Germany, employing the ALADIN-R3B setup for studies of relativistic beams in inverse and full kinematics. An outline of the experimental setup is shown in Fig. 1. A beam of radioactive ^{17}Ne isotopes (500 MeV/u), produced in fragmentation reactions of a ^{20}Ne primary beam, was directed toward lead (199 mg/cm^2), carbon (370 mg/cm^2), and polyethylene (213 mg/cm^2) targets to investigate electromagnetic and nuclear dissociation reactions. The combined measurements with polyethylene and carbon targets allowed us to obtain data for fragmentation of ^{17}Ne on hydrogen. The reaction products were separated according to their mass and charge by the magnetic field of ALADIN (a large-acceptance dipole magnet). Behind ALADIN two separate branches of detectors were used to measure the coordinates of hits, energy loss, and time-of-flight (TOF) of the heavy ions and protons. A tracker routine was employed to get four-momenta of all outgoing charged particles. This analysis requires a precise knowledge of the magnetic field strength inside and outside the magnet, which was measured at several thousands of grid points [13].

A. Observables

The collected reaction events were subdivided into three groups: (i) inclusive detection of oxygen isotopes ($inclusive$), (ii) oxygen isotopes in coincidence with one proton ($p_{\rm mult} = 1$), and (iii) in coincidence with two protons ($p_{\rm mult} = 2$). As will be shown below, we make the following observations:

(1) Events with $p_{\rm mult} = 1$ together with ^{15}O are dominated by one-proton knockout.

(2) Events with $p_{\rm mult} = 1$ and ^{14}O have a complex mechanism of fragmentation.

(3) Events with $p_{\rm mult} = 2$ and ^{15}O are dominated by inelastic scattering with population of excited states in ^{17}Ne and diffractive dissociation.

(4) Events with $p_{\rm mult} = 2$ and ^{14}O reveal distinct features of one-neutron knockout.

The experimental data gave four-momentum vectors for the oxygen isotopes ^{13,14,15}O and for the protons. The analysis of $p_{\rm mult} = 2$ events was done using a Jacobi coordinate system, as described in Ref. [14]. From the four-momentum vectors, the relative energies between ^{13,14,15}O and the observed proton were obtained (E_{fp}). Also the internal energies in the three-body systems ^{13,14,15}O $+ 2p$ (E_{fpp}) were obtained together with the fractional energies $\epsilon_{fp} = E_{fp}/E_{fpp}$.

B. Background

The background stemming from interactions of the beam with the material surrounding the target was obtained in separate measurements with an empty target holder. The probability for detection of one proton (ϵ_{1p}) and two protons (ϵ_{2p}) in the proton-drift chambers (PDCs) was determined experimentally from coincidences with the proton time-of-flight wall, where protons are detected with 100% efficiency in thick plastic scintillators. The probabilities are $\epsilon_{1p} = 0.859(5)$ and $\epsilon_{2p} = 0.58(4)$, and this results in another type of background for events with only one detected proton. There is, namely, a certain probability that two protons may have hit the same wire pair in a PDC, ϵ_w, and such events would be recognized as single-proton events. The probability for this can be estimated to be $\epsilon_w = \epsilon_{1p}^2 - \epsilon_{2p} = 0.16(4)$. Besides, when the energy deposition of a proton in the PDC is below the detection threshold, events with two protons crossing the detector area are misinterpreted as single-proton events with the probability $\epsilon_{2p\to 1p} = 2\epsilon_{1p}(1-\epsilon_{1p})$. The background in $p_{\rm mult} = 1$ events arising from two protons crossing the detector area but misinterpreted as a one-proton event was also taken into account.

C. Geometrical acceptance

After corrections for detection efficiencies and subtraction of background, the differential cross sections need to be corrected for the geometrical acceptance. These corrections for differential cross sections, as functions of E_{fp} for $p_{\mathrm{mult}} = 1$ and E_{fpp} for $p_{\mathrm{mult}} = 2$, were obtained from Monte Carlo simulations, comprising the ALADIN-R3B setup response. Hence, total cross sections for different reaction branches were obtained using the number of detected *inclusive*, $p_{\mathrm{mult}} = 1$, and $p_{\mathrm{mult}} = 2$ events. The basic relation between the total cross sections for *inclusive*, $p_{\mathrm{mult}} = 1$, and $p_{\mathrm{mult}} = 2$ events is

$$\sigma_{\mathrm{incl}} = \frac{\sigma_{\mathrm{incl}}^{\mathrm{raw}}}{A_f} = \frac{\sigma_{1p}^{\mathrm{raw}}}{A_f A_{1p}} + \frac{\sigma_{2p}^{\mathrm{raw}}}{A_f A_{2p}}, \qquad (1)$$

where $\sigma_{\mathrm{incl}}^{\mathrm{raw}}$, $\sigma_{1p}^{\mathrm{raw}}$, and $\sigma_{2p}^{\mathrm{raw}}$ are the respective cross sections for *inclusive*, $p_{\mathrm{mult}} = 1$ and $p_{\mathrm{mult}} = 2$ events corrected for detection efficiency but uncorrected for the geometrical acceptance. A_f, A_{1p}, and A_{2p} are the geometrical acceptances for detection of a fragment, one proton, and two protons. The limited geometrical acceptance A_f results in a suppression of the negative tail of the horizontal momentum component (p_y) and was obtained from the fit by only using its positive values. A_f was found to be 1.00 for detection of ^{15}O, 0.90(5) for ^{14}O, and about 0.5 for ^{13}O. As an example, Fig. 2 shows this for the CH_2 target.

Equation (1) demonstrates that the absolute values of the total cross sections for different branches of Coulomb and nuclear dissociations of ^{17}Ne can be obtained by only using the experimentally determined quantities without Monte Carlo simulations, which generally are used for this purpose. Monte Carlo simulations suffer, however, from some unavoidable approximations for the input data describing kinematic properties of fragments in the final state. In particular, when the GENBOD random event generator [15] is used, it generates multiparticle dissociation events according to the Lorentz-invariant phase space, while the present experiment has shown that sequential proton emission, with population of excited states in ^{16}F, is essential.

The PDCs allow for detection of protons with transverse momenta up to $\approx$70 MeV/c. The shapes of the transverse momentum distributions for protons obtained from $p_{\mathrm{mult}} = 1$ and $p_{\mathrm{mult}} = 2$ events were found to be indistinguishable within the statistical uncertainties (see Fig. 3).

This thus gives evidence that $A_{2p} = A_{1p}^2$. The geometrical acceptances for single-proton events in coincidence with ^{14,15}O fragments (A_{1p}) were determined for each target separately by using Eq. (1) and assuming that $A_{2p} = A_{1p}^2$. The resulting values demonstrate an insensitivity to the target material with $\chi^2 = 0.34$ for ^{15}O and $\chi^2 = 0.68$ for ^{14}O. Here χ^2 is the weighted sum of squared differences between A_{1p} obtained for the individual targets and their weighted mean value. The weighted mean value of A_{1p} is 0.744(10) and $A_{1p}^2 = 0.553(15)$. The assumption that $A_{2p} = A_{1p}^2$ was checked by using explicitly Eq. (1) and the data from different targets. The corresponding A_{1p} weighted mean value is 0.759(30), $A_{2p} = 0.514(52)$, confirming the assumptions of target independence and $A_{2p} = A_{1p}^2$ is valid within an uncertainty lower than 10%. The comparison of obtained acceptance factors to the Monte Carlo results shows that the approximations used to describe the fragmentation mechanism are acceptable.

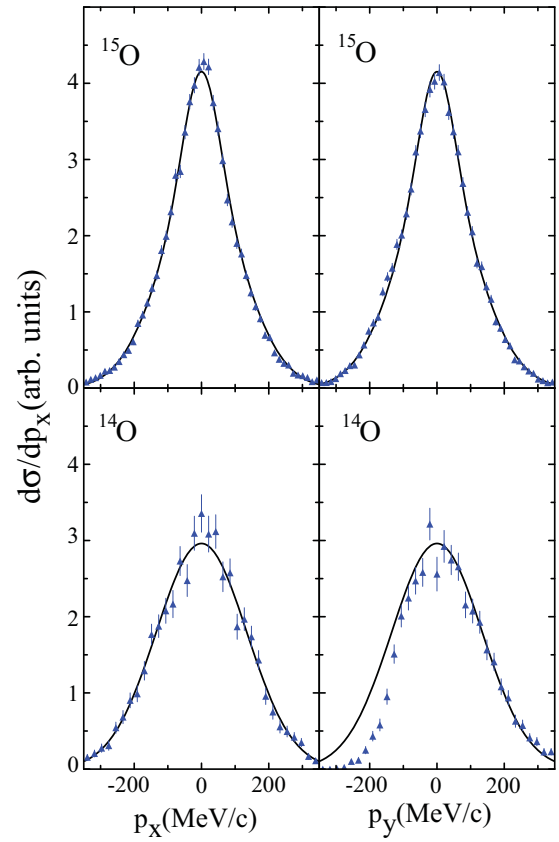

FIG. 2. Momentum distributions of ^{15}O fragments, $p_{\mathrm{mult}} = 1$, in the transverse direction toward the ^{17}Ne beam (p_x – vertical, p_y – horizontal). The limited acceptance of the ALADIN spectrometer results in a suppression of events with negative values of p_y. The displayed data were obtained with the CH_2 target.

The ^{15}Ne from $^{13}\mathrm{O} + 2p$, the ^{16}Ne from $^{14}\mathrm{O} + 2p$ triple coincidences and inelastic scattering with excitation of narrow resonances in ^{17}Ne have been analyzed and the results were

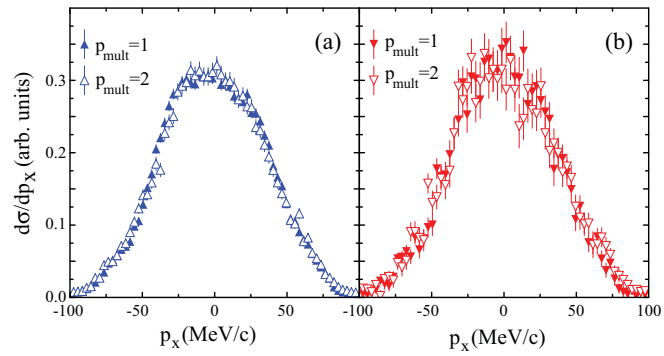

FIG. 3. Comparison between transverse momentum distributions of protons when ^{15}O is registered with different multiplicities of protons crossing the detector area. (a) Data obtained with a CH_2 target. (b) Results obtained with a Pb target. The distributions were corrected for background and normalized to the same integral value.

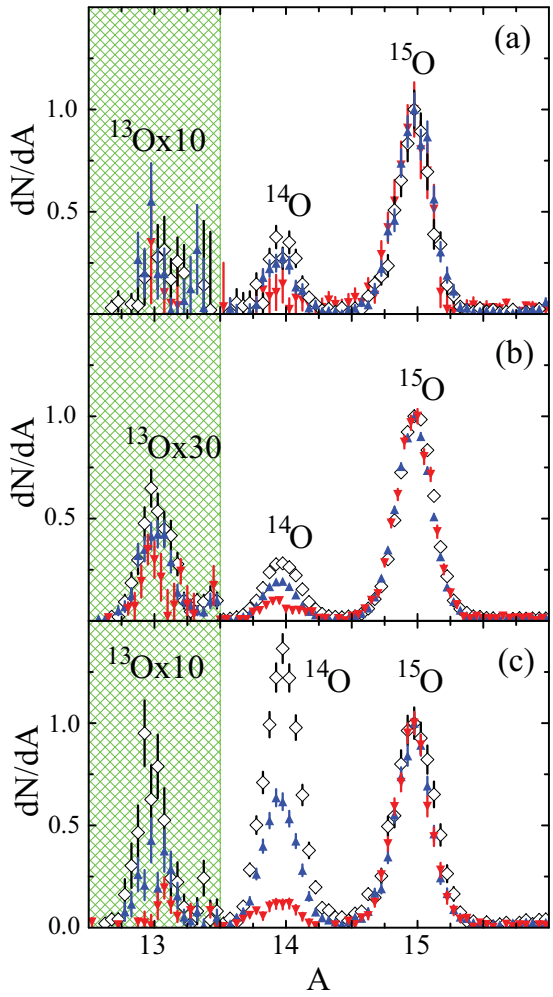

FIG. 4. Mass spectra of oxygen isotopes, dN/dA, obtained in the dissociation of 500 MeV/u ^{17}Ne impinging on hydrogen (⋄), carbon (blue, ▲), and lead (red, ▼) targets. The distributions were obtained in inclusive detection of oxygen isotopes (a), and in coincidences with one or two protons: ^{13,14,15}O+1p (b), and ^{13,14,15}O+2p (c). Distributions in (b) were corrected for misidentification of two protons as a single one (see text). The empty-target background was subtracted. The scale of the dN/dA distribution is fixed by normalizing the ^{15}O peaks to unity. The ^{13}O data (hatched region) were scaled up by the shown factors.

published in Refs. [9,16,17]. The present paper is devoted mainly to the disentanglement of different reaction branches in the dissociation of ^{17}Ne, and to the electromagnetic dissociation resulting in a continuous internal energy spectrum in the ^{15}O − 2p three-body system.

III. FRAGMENTATION MECHANISMS

Figure 4 demonstrates the quality of isotope separation and, together with the transverse momentum distributions of oxygen isotopes in Fig. 5, reveals the salient features of different fragmentation mechanisms depending on the reaction target and proton multiplicity. Table I presents the FWHM of the momentum distributions. The widths of the ^{15}O momentum

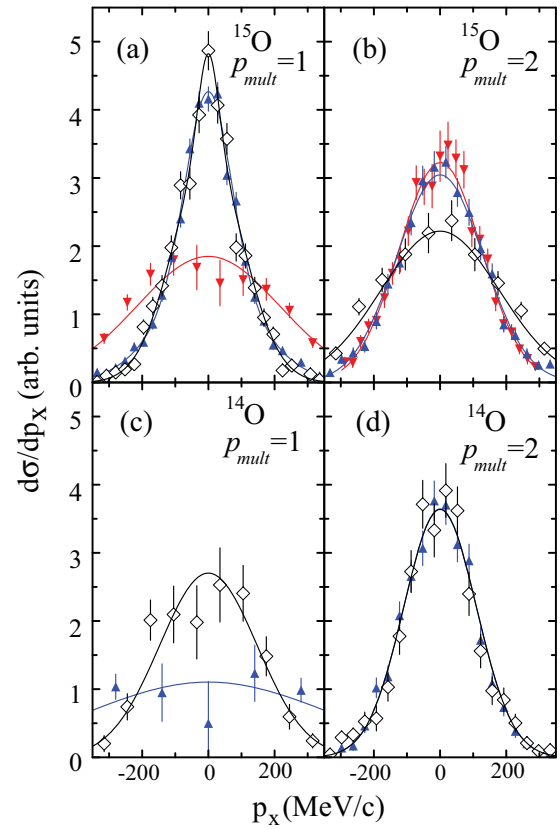

FIG. 5. Comparison of transverse momentum distributions for ^{15}O and ^{14}O fragments, and different multiplicities of protons crossing the detector area, $p_{\rm mult} = 1$ and $p_{\rm mult} = 2$. The Pb data in frames (c) and (d) were left out due to too low statistics. Notation for the different targets is the same as in Fig. 4.

distributions for $p_{\rm mult} = 1$ are narrow for the light targets but about a factor of 2 larger for the lead target [see Fig. 5(a)]. For all these events, one proton exhibits such a large momentum transfer that it is scattered outside the range of the proton detectors, and accordingly we attribute them to the one-proton knockout mechanism. Single-proton knockout results in the population of excited states in ^{16}F. The comparison of the E_{fp} spectra obtained with different targets, shown in Fig. 6, illustrates that the relative population of states in ^{16}F is independent of the reaction target. In the Pb case, proton knockout takes place deep inside the Coulomb field resulting in a strong deflection of the charged particles. The proton-unstable ^{16}F fragment is passing the region of Coulomb repulsion as one

TABLE I. FWHM in MeV/c for fragment momentum distributions. The data are corrected for the experimental resolution.

Target	Fragment	$p_{\rm mult} = 1$	$p_{\rm mult} = 2$
Hydrogen	^{15}O	142(10)	362(15)
	^{14}O	290(15)	213(8)
Carbon	^{15}O	152(14)	301(6)
	^{14}O	broad	213(5)
Lead	^{15}O	430(22)	285(6)

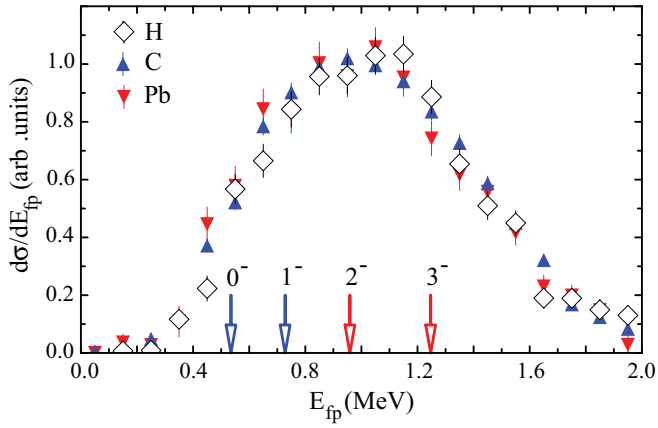

FIG. 6. Comparison of relative energy spectra E_{fp} obtained in coincidence between ^{14,15}O and a proton for $p_{\mathrm{mult}} = 1$ for the three targets. The arrows show the excitation energies of resonance states in ^{16}F.

single object and its decay takes place outside the region of the strong Coulomb field, since the widths of the lowest four resonances in ^{16}F are less than 100 keV, corresponding to a 1500-fm distance traveled by the excited ^{16}F during the resonance lifetime. The widths of ^{15}O momentum distribution shown in Fig. 4(a) for the Pb target is broader than for the lighter targets. The reaction mechanism is interpreted to mainly be due to (1) inelastic scattering with excitation of ^{17}Ne states and (2) diffractive dissociation to $^{15}\mathrm{O} + 2p$ without a strong final-state interaction. In this case the two protons are emitted in the forward direction.

The data obtained for ^{14}O in the $p_{\mathrm{mult}} = 1$ case, shown in Fig. 5(c), suggest a complex fragmentation mechanism. The momentum distributions are broad for all targets.

One notes in Fig. 4(c) a significant decrease in the yield of ^{15}O relative to ^{14}O in the $p_{\mathrm{mult}} = 2$ case with light targets. This is also seen in the ratio $R(x) = \sigma(^{15}\mathrm{O})/\sigma(^{14}\mathrm{O})$ in Table II: $R(H) = 0.95(16)$, $R(C) = 1.18(10)$, and $R(Pb) = 6.11(68)$, where the given uncertainties are statistical. The inelastic scattering and diffractive dissociation reaction mechanisms are predominant for the lead target, while a nucleon knockout mechanism is more probable for the hydrogen and carbon targets.

TABLE II. Total cross sections (mb) for fragmentation of ^{17}Ne in different targets. The data are corrected for background, detection efficiency, and geometrical acceptance. The indicated uncertainties are statistical.

Target	Fragment	σ_{incl}	σ_{1p}	σ_{2p}
Hydrogen	^{15}O	52.0(3.0)	42.3(1.6)	8.75(59)
	^{14}O	20.4(2.9)	10.4(1.1)	9.7(1.5)
Carbon	^{15}O	117.5(4.0)	98.6(1.6)	20.68(68)
	^{14}O	30.4(3.1)	11.61(87)	17.5(1.3)
Lead	^{15}O	534(22)	296.9(8.5)	227.4(6.9)
	^{14}O	63(20)	17.8(4.1)	37.2(4.0)

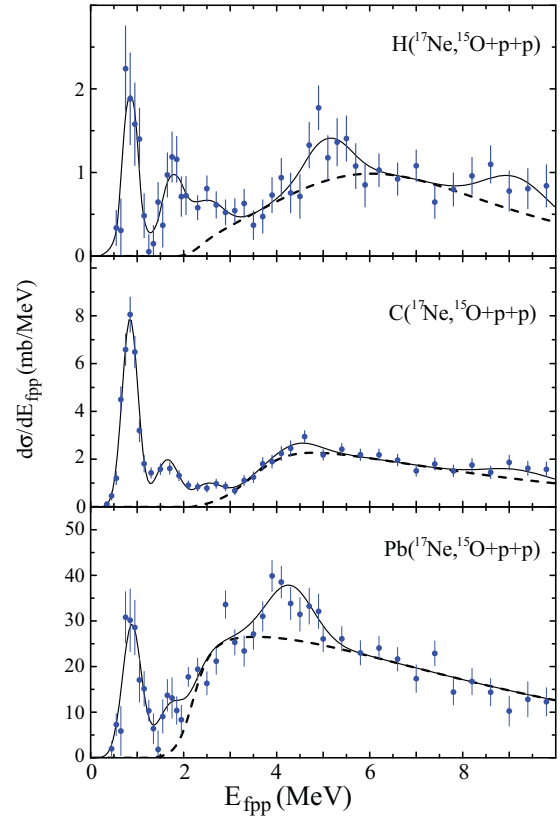

FIG. 7. Relative energy spectra for the $^{15}\mathrm{O} + 2p$ system obtained with hydrogen, carbon, and lead targets. The full drawn curves represent excited states superimposed on a smooth contribution from diffractive dissociation (dashed curves) [9].

The momentum distributions for ^{14}O with $p_{\mathrm{mult}} = 2$, shown in Fig. 5(d), are significantly narrower than for ^{14}O with $p_{\mathrm{mult}} = 1$ [Fig. 5(c)]. This is evidence for a neutron knockout mechanism, which leads to the unbound nucleus ^{16}Ne decaying via two-proton emission with both protons flying in the forward direction.

The total cross sections for fragmentation of ^{17}Ne on different targets corrected for background, detection efficiency, and geometrical acceptance are presented in Table II.

IV. RELATIVE ENERGY SPECTRA

The experimental $^{15}\mathrm{O} + p + p$ relative-energy spectra shown in Fig. 7 are due to excited states in ^{17}Ne superimposed on a smooth contribution to the spectrum from diffractive dissociation (dashed curves) [9]. The nuclear and electromagnetic excitations of narrow resonances in ^{17}Ne were discussed in Ref. [9] together with the three-body correlations at low energies for the E_{fpp} up to 3.0 MeV. However, as seen in Fig. 7, the fragmentation shows also a strong contribution at higher energies where there is no pronounced resonance structure.

The fractional energy distributions in different relative energy regions are shown in Figs. 8 and 9. These distributions were fitted assuming sequential proton emission with population of the lowest four negative parity states in ^{16}F. Population of positive parity states is, however, also required at

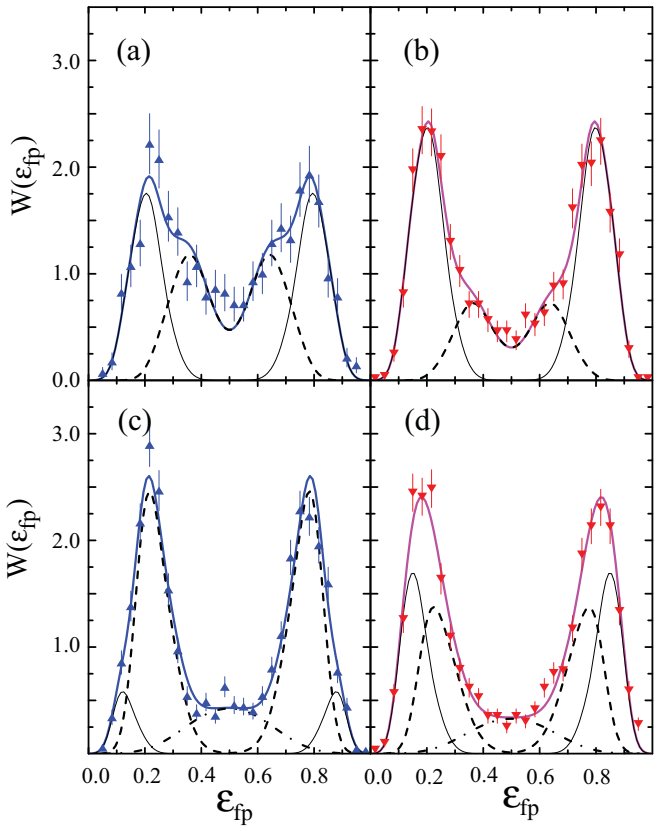

FIG. 8. Fractional energy spectra in $3.0 \leqslant E_{fpp} \leqslant 3.8$ MeV in (a) and (b) and $3.8 \leqslant E_{fpp} \leqslant 5.0$ MeV [(c), (d)] from CH_2 [(a), (c)] and Pb [(b), (d)] targets. The least-square fits to the data, assuming population of ^{16}F$(0^-,1^-)$ states (thin solid lines), ^{16}F$(2^-,3^-)$ (dashed lines), and a genuine three-body decay (dashed-dotted lines), are shown.

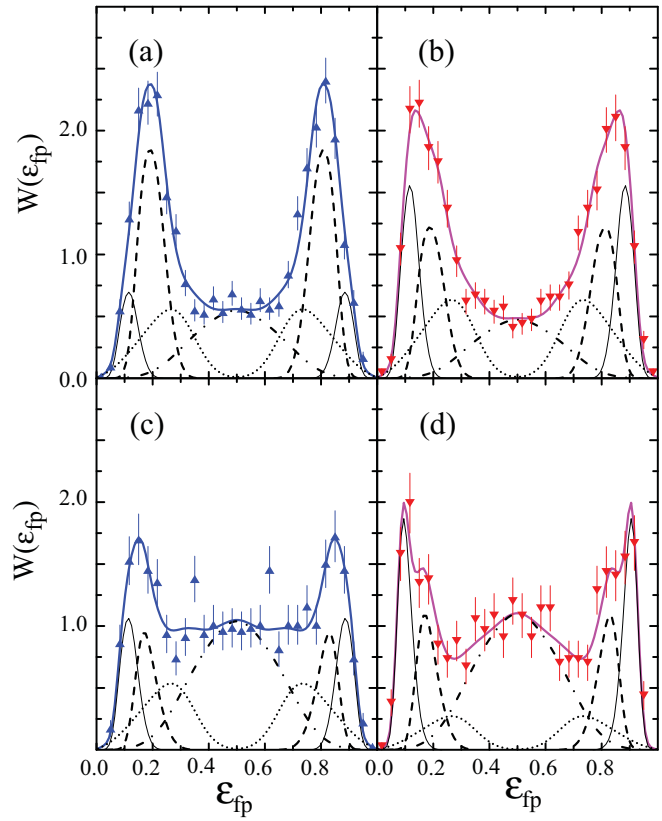

FIG. 9. Fractional energy spectra in $5.0 \leqslant E_{fpp} \leqslant 6.5$ MeV in (a) and (b) and $6.5 \leqslant E_{fpp} \leqslant 8.0$ MeV [(c), (d)] from the CH_2 [(a), (c)] and Pb target [(b), (d)]. The least-square fits to the data, assuming population of ^{16}F$(0^-,1^-)$ states (thin solid lines), ^{16}F$(2^-,3^-)$ (dashed lines), ^{16}F(I^+) states (dashed lines), and a genuine three-body decay (dashed-dotted lines), are shown.

$5.0 < E_{fpp} < 8.0$ MeV. The signatures of genuine three-body decays start to become evident at $E_{fpp} > 3.8$ MeV. Only the amplitudes of the components were used as free parameters in the fits.

The shape of the $W(\epsilon_{fp})$ distribution for a genuine three-body decay was described assuming $[s^2] \rightarrow [sp]$ as the dominating transition:

$$W(\epsilon) \sim \sum_{i,j=1,2}^{i\neq j} e^{-G(\frac{1}{\sqrt{E_i}}+\frac{1}{\sqrt{E_j}})} \epsilon^{\ell_i+\frac{1}{2}}(1-\epsilon^{\ell_j+\frac{1}{2}}), \qquad (2)$$

where E_1, ℓ_1 (E_2, ℓ_2) are relative ^{15}O-p energies and angular momenta for the protons. Here the exponential is the Gamow penetrability factor, where G was obtained from a fit to the penetrability factor as a function of energy, calculated using the RCWFN code [18], and where the last two terms represent the phase space.

The lowest states 0^- and 1^- in ^{16}F have the structure $^{15}\mathrm{O}(1/2^-) \otimes (1s_{1/2})$ while $^{15}\mathrm{O}(1/2^-) \otimes (0d_{5/2})$ characterizes the 2^- and 3^- states. The widths of all four states are consistent with single-proton states [19]. Population of d states in ^{16}F have larger probability than s states for light targets, while in reactions in the lead target mainly s states are populated. The relative contributions from different branches in different E_{fpp} energy regions for CH_2 and Pb targets are shown in Table III.

V. ELECTROMAGNETIC DISSOCIATION

The electromagnetic dissociation (EMD) cross section was obtained by subtracting the nuclear dissociation contribution from the $d\sigma/dE$(lead) spectrum. This contribution was taken as the $d\sigma/dE$(carbon) contribution scaled by a factor of 1.84(20). This scaling factor was determined experimentally

TABLE III. Decay branches (%) in the fragmentation of ^{17}Ne on CH_2 and Pb targets. ^{16}F(I^+) denotes positive parity states in ^{16}F at excitation energies $3.7 < E^* < 4.4$ MeV. The indicated uncertainties are statistical.

ΔE	^{16}F$(0^- + 1^-)$	^{16}F$(2^- + 3^-)$	^{16}F(I^+)	3-body decay
3.0–3.8	53(6)/68(5)	47(6)/32(4)		<5/<5
3.8–5.0	22(3)/45(4)	63(5)/42(4)		15(1)/13(1)
5.0–6.5	12(2)/25(3)	39(4)/27(4)	29(3)/30(4)	20(2)/18(2)
6.5–8.0	9(3)/20(4)	29(4)/24(5)	32(3)/14(3)	30(3)/42(3)
8.0–10.	7(4)/12(5)	35(5)/24(5)		58(7)/64(8)

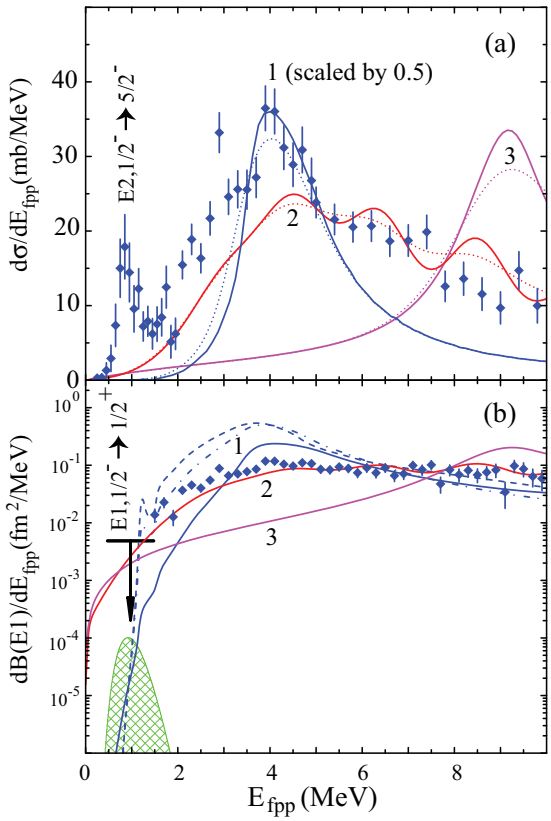

FIG. 10. (a) Differential cross section for electromagnetic dissociation. (b) Dipole strength function $dB(E1)/dE_{fpp}$. The experimental data are shown by filled rhombuses with the indication of statistical uncertainties. Results of theoretical calculation using different models are marked by 1 for [11] [blue solid line - $P(s^2) = 5\%$, dashed line - $P(s^2) = 48\%$, dashed-dotted line- $P(s^2) = 73\%$], by 2(red) for [22], and by 3 (magenta) for [23]. The dotted lines in (a) demonstrate the influence of experimental energy resolution. The upper limit for ^{17}Ne(g.s.) $\rightarrow$ ^{17}Ne($1/2^+$) resonance transition from [9] is shown. The hatched zone shows the position of the Gamow window for ^{15}O$(2p,\gamma)^{17}$Ne as a function of E_{fp} at 1 GK temperature.

in Ref. [9] by assuming that the electromagnetic dissociation of ^{17}Ne to ^{14}O has a negligible cross section. The scaling factor is close to the ratio between the sums of projectile and target matter radii, reflecting that the nuclear disintegration is of surface character. The EMD cross section with ^{14}O in the final state is close to zero, 1.6(6.6) mb, as expected, and thus confirming the value of the scaling factor. The EMD cross section for ^{15}O as the reaction product was 305(11) mb, with 115(9) mb in the channel with $p_{\rm mult} = 1$. From the experimental data $d\sigma/dE_{fpp}$ and from that the dipole-strength function $dB(E1)/dE_{fpp}$ was calculated by using the virtual photon method [20,21]. The virtual photon numbers were taken from [11]. The obtained differential cross section for electromagnetic dissociation is shown in Fig. 10(a), and the corresponding dipole-strength function $dB(E1)/dE_{fpp}$ in Fig. 10(b). The curves 1 (blue), 2 (red), and 3 (magenta) were obtained in calculations using three different models.

The calculations for curve 1 were based on a three-body model in which only the ^{15}O-p interaction is taken as important, "the one final-state interaction model" (OFSI) [11]. The results were obtained assuming different weights of the (s^2) component in the ^{17}Ne(g.s.): 5%, 48%, and 73%. The $E1$ strength function was calculated for $[s^2] \rightarrow [sp]$ and $[d^2] \rightarrow [dp]$ transitions. The calculated cross section increases strongly with the increasing $P(s^2)$. In order to get agreement with the experimental data in the region around 4 MeV (maximum of the cross section) the following scaling factors would be required: 0.5 for $P(s^2) = 5\%$, 0.25 for $P(s^2) = 48\%$, and 0.22 for $P(s^2) = 73\%$.

The curves labeled 2 in Fig. 10 show the EMD cross section and $dB(E1)/dE_{fpp}$ distribution obtained from [22]. The $E1$ strength was calculated for ^{17}Ne assuming a $^{15}\mathrm{O} + 2p$ structure with s- and d-wave probabilities $P(s^2) = 16\%$ and $P(d^2) = 76\%$, where the two valence protons are excited from the 0^+ ground-state configuration to 1^- continuum states.

Finally each curve 3 in Fig. 10 shows results obtained from [23]. These calculations were made in the framework of the Hartree-Bogoliubov theory and in a relativistic quasiparticle random-phase approximation. The proton pygmy dipole resonance (PDR) was predicted at $E_{fpp} = 9.26$ MeV. A similar result has been obtained in [24] within a shell model with the self-consistent Skyrme-Hartree-Fock wave functions where the PDR was predicted at around 10 MeV. The common feature for all three calculations is an underestimate of the dissociation cross section in the energy region below 3 MeV. However, as shown in Fig. 10(a), the probability for excitation of the $5/2^-_1$ state at resonance energy 0.83 MeV by an $E2$ transition is large. In our earlier study of population of narrow resonances in ^{17}Ne [9], evidence was found for $3/2^-_2$ and $5/2^-_2$ states at resonance energies 1.76 and 2.48 MeV, respectively. Also, two additional states with $\mathrm{I}^\pi = 3/2^-$ or $5/2^-$ were observed in the mirror nucleus ^{17}N at excitation energies 4.4 and 5.5 MeV [25], which would indicate the presence of isobar-analog states in ^{17}Ne at resonance energies $\approx$3 and $\approx$4 MeV. These facts indicate that the $E2$ transitions are not negligible in the dissociation of ^{17}Ne. The result obtained in [22] is within spitting distance of the experimental spectrum above 5 MeV.

The hatched region in Fig. 10(b) shows the position of the Gamow window for ^{15}O$(2p,\gamma)^{17}$Ne at 1 GK temperature. The reaction rate is very sensitive to the $dB(E1)/dE$ value in this energy region where the values obtained in Refs. [22,23] are, by several orders of magnitude, larger than those in [11]. As stated in [10], a significant part of the $E1$ strength goes to the ^{17}Ne($1/2^+$) resonance at 0.975 MeV above the $^{15}\mathrm{O} + 2p$ threshold. The upper limit for ^{17}Ne(g.s.) $\rightarrow$ ^{17}Ne($1/2^+$) transition from [9] is shown in Fig. 10.

A combination of several models, based on the three-body structure of ^{17}Ne, was used in recent calculations [26]. The $E1$ strength function was obtained assuming $P(s^2) = 48\%$ for ^{17}Ne(g.s.). The $E1$ strength function is close to the result of the OFSI model [11]. The calculated cross section of the $E1$ excitation, $\sigma(E1) = 386$ mb [26], is close to the one obtained in the present experiment. However, the ratio between the cross sections leading to production of ^{16}F in s wave, $\sigma(E1,s) = 368$ mb, and d wave, $\sigma(E1,d) = 18$ mb, is 20, while the experimental ratio does not exceed a factor of 2.

VI. SUMMARY

A systematic study of nuclear and electromagnetic dissociation of ^{17}Ne using light and heavy targets has been performed. The data allowed us to extract information from reactions with targets of H, C, and Pb. It is shown that absolute values for nuclear and electromagnetic dissociation can be obtained solely by using experimentally measured quantities.

Different fragmentation branches were identified including the population of both negative, and, at higher energy, positive parity states in ^{16}F. It is found that the relative population of the states in ^{16}F in proton knockout reactions is independent of the reaction target. A contribution from genuine three-body decay to $^{15}\mathrm{O} + 2p$ is also observed.

The data allowed extracting the electromagnetic dissociation differential cross section as well as the dipole-strength function up to 10 MeV for ^{17}Ne. Comparisons of five different model calculations [11,22–24,26] to experimental data were performed. None of these give, however, a satisfactory agreement with the experimental data. The calculations [22] with the ^{17}Ne(g.s.) structure based on a three-body model are closest to the experimental data. However, the experiments give indications that quadrupole excitations are not negligible. A surprising fact is that two different calculations based on the same assumption of the ^{17}Ne(g.s.) structure [11,22] gave fairly different results. The data obtained in the present experiment may help facilitate the development of a paradigmatic model for the description of the fragmentation process.

ACKNOWLEDGMENTS

The authors are thankful to N. Shulgina, T. Oishi, and Y. Tian for making available numerical data of the $E1$ strength for ^{17}Ne and to M. Zhukov and G. Nyman for discussions. This project is supported by NAVI, GSI-TU Darmstadt cooperation, HIC for FAIR, EMMI, and BMBF and from DFG through Grant No. SFB1245 and from BMBF via Project No. 05P15RDFN1, and from the Spanish Ministry by research grant FPA2015-64969-P. C.A.B. acknowledges support by the US DOE Grant No. DE-FG02-08ER41533 and the US NSF Grant No. 1415656.

[1] L. V. Chulkov, B. Jonson, and M. V. Zhukov, Eur. Phys. J. A **51**, 1 (2015).
[2] K. Riisager, Phys. Scr. T **152**, 014001 (2013).
[3] R. E. Warner, J. H. Kelley, P. Zecher, F. D. Becchetti, J. A. Brown, C. L. Carpenter, A. Galonsky, J. Kruse, A. Muthukrishnan, A. Nadasen, R. M. Ronningen, P. Schwandt, B. M. Sherrill, J. Wang, and J. S. Winfield, Phys. Rev. C **52**, R1166 (1995).
[4] M. J. G. Borge *et al.*, Phys. Lett. B **317**, 25 (1993).
[5] R. E. Warner *et al.*, Nucl. Phys. A **635**, 292 (1998).
[6] M. V. Zhukov and I. J. Thompson, Phys. Rev. C **52**, 3505 (1995).
[7] M. Wang, G. Audi, A. H. Wapstra, F. G. Kondev, M. MacCormick, X. Xu, and B. Pfeiffer, Chin. Phys. C **36**, 1603 (2012).
[8] H. T. Fortune and R. Sherr, Phys. Lett. B **503**, 70 (2001).
[9] J. Marganiec *et al.*, Phys. Lett. B **759**, 200 (2016).
[10] J. Casal, E. Garrido, R. de Diego, J. M. Arias, and M. Rodríguez-Gallardo, Phys. Rev. C **94**, 054622 (2016).
[11] L. V. Grigorenko, K. Langanke, N. B. Shulgina, and M. V. Zhukov, Phys. Lett. B **641**, 254 (2006).
[12] J. Görres, M. Wiescher, and F. K. Thielemann, Phys. Rev. C **51**, 392 (1995).
[13] R. Plag (private communication).
[14] M. Meister, L.V. Chulkov, H. Simon, T. Aumann, M. J. G. Borge, T. W. Elze, H. Emling, H. Geissel, M. Hellström, B. Jonson, J. V. Kratz, R. Kulessa, Y. Leifels, K. Markenroth, G. Münzenberg, F. Nickel, T. Nilsson, G. Nyman, V. Pribora, A. Richter, K. Riisager, C. Scheidenberger, G. Schrieder, O. Tengblad, and M. V. Zhukov, Phys. Rev. Lett. **91**, 162504 (2003).
[15] F. James, Monte Carlo Phase Space, CERN 68-15, 1968 (unpublished).
[16] J. Marganiec *et al.*, Eur. Phys. J. A **51**, 9 (2015).
[17] F. Wamers *et al.*, Phys. Rev. Lett. **112**, 132502 (2014).
[18] A. R. Barnett, D. H. Feng, J. W. Steed, and L. J. B Goldfarb, Comput. Phys. Commun. **8**, 377 (1974).
[19] C. R. Hoffman, B. P. Kay, and J. P. Schiffer, Phys. Rev. C **94**, 024330 (2016).
[20] C. A. Bertulani and G. Baur, Phys. Rep. **163**, 299 (1988).
[21] C. A. Bertulani and A. M. Nathan, Nucl. Phys. A **554**, 158 (1993).
[22] T. Oishi, K. Hagino, and H. Sagawa, Phys. Rev. C **84**, 057301 (2011).
[23] Z. Y. Ma and Y. Tian, Sci. China Phys., Mech. Astron. **54**, 49 (2011).
[24] H.-L. Ma, B.-G. Dong, Y.-L. Yan, H.-Q. Zhang, and X.-Z. Zhang, Phys. Rev. C **85**, 044307 (2012).
[25] D. R. Tilley, H. R. Weller, and C. M. Cheves, Nucl. Phys. A **564**, 1 (1993).
[26] Yu. Parfenova, L. V. Grigorenko, I. A. Egorova, N. B. Shulgina, and M. V. Zhukov, J. Phys.: Conf. Ser. **665**, 012047 (2016).